Revision 2

Mineralogical characterization and formation of Fe-Si oxyhydroxide deposits from modern seafloor hydrothermal vents

Zhilei Sun [a,b], Huaiyang Zhou [c*], G. P. Glasby [a,b], Zhixue Sun[d], Qunhui Yang [c], Xijie Yin[e], Jiwei, Li [f]

[a] *Key Laboratory of Marine Hydrocarbon Resources and Environmental Geology, Ministry of Land and Resources, 266071, Qingdao, China*

[b] *Qingdao Institute of Marine Geology, 266071, Qingdao, China*

[c] *School of Ocean and Earth Sciences, Tongji University, Shanghai, 200092, China*

[d] *School of Petroleum Engineering, China University of Petroleum, Qingdao, 266555, China*

[e] *Third Institute of Oceanography State Oceanic Administration, Xiamen, 361005, China*

[f] *Faculty of geoscience and environment engineering, Southwest Jiaotong University, Chengdu, 614202, China*

∗ *Corresponding author: E-mail:* sunmarine@yeah.net, *Tel.: +86 (532) 80778373, Fax: +86 (532) 85720553.*

ABSTRACT

We have studied mineralogical characteristics of Fe-Si oxide precipitates from hydrothermal fields of the Valu Fa Ridge, Lau Basin, especially the role that the neutrophilic Fe-oxidizing bacteria played in their formation, using a variety of analytical techniques (XRD, SEM, EPMA, TG/DTA and FTIR). According to this examination, the Fe-Si oxide formation can be divided into two stages. At the initial stage, the Fe-oxidizing bacteria bound and oxidized Fe^{2+} into Fe^{3+} in order to fix CO_2, triggering precipitation of Fe-oxyhydroxide (ferrihydrite) and construction of a loose network of Fe-rich filaments. Subsequently, the decreased porosity of the network resulting from the gradual growth of the filaments led to a decline in the mixing between seawater and the hydrothermal fluids. Then the conductive cooling of the network resulted in saturation of the dissolved Si with respect to amorphous silica. As a result, significant precipitation of opal-A occurred through inorganic polymerization. However, part of the silica was immobilized by bonding to Fe-OH functional groups and yielded unpolymerized silica which is characterized by Fe-O-Si bond. Owing to the incorporation of Si into the ferrihydrite structure and its adsorption on the ferrihydrite surface, the modern hydrothermal Fe-Si oxides are thermally stable. DSC

Always consult and cite the final, published document. See http://www.minsocam.org or GeoscienceWorld

measurements indicate the full segregation of cristobalite from hematite at about 800 °C in an O_2 atmosphere. These observations indicate that primary alternating Si- and Fe-rich layers may be absent in the Archean ocean and thus provide potential clue to unravel the precipitation and diagenetic mechanisms of Precambrian banded iron formations (BIF).

Keywords Lau Basin; hydrothermal Fe-Si oxides; banded iron formations; neutrophilic Fe-oxidizing bacteria

Introduction

Fe-Si oxide/oxyhydroxide (hereafter referred to as Fe-Si oxide) is identified as a common constituent of modern seafloor hydrothermal vent systems. It occurs as chimneys, irregularly shaped edifices, mounds and interstitial precipitates filling cracks between lava flows (Hekinian et al., 1993). Following the discovery of modern hydrothermal vents in late 1970s (Corliss et al., 1979), Fe-Si oxide precipitates have been documented in hydrothermal systems globally. Previous studies have shown that Fe-Si oxide precipitates are favored by relatively low-temperatures (<100 ºC) in chimney structures and under diffuse flow conditions. This type of precipitate is probably comprised of amorphous silica and poorly crystalline phases of which ferrihydrite is the most pervasive. Sometimes crystalline iron-rich silicates such as nontronite are also found in these precipitates. Fe-Si oxide deposits are now considered to be a result of either hydrothermal plume fallout of Fe-Si oxyhydroxide precipitates or the mass wasting and erosion of primary submarine massive sulfides. Textural and molecular biological evidences also suggest that microorganisms (for instance iron-oxidizing bacteria) are essential in both these processes (e.g., Boyd and Scott, 2001; Edwards et al., 2003, 2004, 2011；Little et al., 2004；Kato et al., 2009；Langley et al., 2009; Toner et al., 2009).

Three main neutrophilic Fe-oxidizing bacteria have been identified by molecular analysis from modern hydrothermal Fe-Si oxyhydroxide deposits (Emerson et al., 2007；Davis et al., 2008；Hodges et al., 2009；Kato et al., 2009；Langley et al., 2009). Although abiogenic mechanisms for Fe-Si filament formation have been proposed (Hopkinson et al., 1998) and similar structures of filaments have even formed under abiogenic conditions (García-Ruiz et al. 2002, 2003), several questions still remain unsolved. For example, abiogenic mechanisms alone cannot explain the

Always consult and cite the final, published document. See http://www.minsocam.org or GeoscienceWorld

formation of hollow cylinders in the Fe oxides, the straight, twisted and branching morphologies of the filaments, the internal septate structures and the occurrence of terminal knobs (Little et al., 2004). Rather, these complex microstructures indicate that the precipitation of Fe oxide is a complex process, probably involving both biotic and abiotic pathways. In addition, some studies have been carried out to determine the silica precipitation (Juniper and Fouquet., 1988; Herzig et al., 1988; Kristall., 2006) and Fe-Si coprecipitation of hydrothermal fluids (Fein et al., 2002; Yee et al., 2003; Konhauser et al., 2007; Posth et al., 2008) to investigate the possible affinity and relationship of these deposits to the Precambrian banded iron formation (BIF).

It is noteworthy that in natural environment, Fe-Si oxide is not a simple mixture of Fe-oxyhydroxide and amorphous or poorly crystalline silica. As Si has a high affinity for the Fe-OH functional group of Fe oxides, it is likely that Si interacts with the growth of Fe oxide crystals, resulting in the formation of Si-containing ferrihydrites (Campbell et al., 2002). A number of studies have shown that much of the Si may have been incorporated into the ferrihydrite structure (Eggleton and Fitzpatrick, 1988; Waychunas, 1991; Jambor and Dutrizac, 1998; Boyd and Scott, 1999), probably replacing Fe in tetrahedral site up to 0.214 mol% in many natural ferrihydrites (Carlson and Schwertmann, 1981; Childs et al., 1993). However, debates still exist about this structure model. For instance, several investigators have argued that the Si in ferrihydrite is adsorbed on its surface from the surrounding aqueous solution, probably as the anion $HSiO_4^{3-}$ (Zhao et al., 1994; Cismasu et al., 2011). The main reason is the considerable difference in ionic radii between Si^{4+} and Fe^{3+} (0.26 Å for $^{IV}Si^{4+}$ and 0.49 Å for $^{IV}Fe^{3+}$; Shannon 1976) and the limited number of tetrahedral sites in the average ferrihydrite structure (ideally 20% of the total Fe sites; Cismasu et al., 2011). According to this model, Si was suggested to hinder the growth of ferrihydrite crystallites by attaching to newly formed iron oligomers during polymerization and by inhibiting the cross-linking of edge-sharing Fe oligomers, whereas at higher concentrations, silica is thought to polymerize and form a shell around the ferrihydrite (Seehra et al., 2004). In this paper, the term “Si-ferrihydrite” is reserved for ferrihydrites containing unpolymerized Si.

Previous research on hydrothermal Fe-Si oxide precipitates was mostly aimed at identifying microorganisms involved in the precipitation. By contrast, detailed mineralogical and geochemical characteristics of modern hydrothermal Fe-Si deposits still need further investigation; our present

Always consult and cite the final, published document. See http://www.minsocam.org or GeoscienceWorld

knowledge of Fe-Si oxide relies mainly on previous analyses of analogs in freshwater, soils and terrestrial hot springs. In addition, the amorphous or poorly crystalline nature of Fe-Si oxyhydroxide precipitates makes X-ray diffraction (XRD) studies alone insufficient for their characterization (Zhao et al., 1994; Garcia-Valles et al., 2008). Other analytical methods need to be employed.

The main goal of this work is to characterize the mineralogical and geochemical nature of Fe-Si oxide precipitates from the hydrothermal fields of the Valu Fa Ridge, Lau Basin. Specifically, we have used XRD, scanning electron microscopy (SEM), thermogravimetry and differential thermal analysis (TG-DTA), Fourier Transform infrared spectroscopy (FTIR), electron probe micro-analysis (EPMA) and energy dispersive spectral (EDS) analyses to determine the factors controlling the precipitation and thermal stability of modern hydrothermal Fe-Si oxides and particularly to address the biogenic mechanism of deposition of Fe-Si oxides. In addition, the obtained results may have implications for BIF formation.

2. Geological Setting

The Lau Basin is a triangular depression over 1000 km long and approximately 450 km wide in the north (at 15°S), narrowing to about 200 km in the south (25°S). This active back-arc basin has been opening over the last 6 Ma (Hawkins, 1995) through rapid clockwise rotation (7°/Ma) of the Tonga Arc; the Euler pole of the motion for the rotation lies at about 24°S (Bevis et al., 1995). The basin is bordered to the east by the Tonga Ridge and to the west by the Lau Ridge. The Lau Ridge is a remnant volcanic arc abandoned by spreading in the Lau Basin and was active between the mid-Miocene and early Pliocene (approximately 15–5 Ma; Hawkins, 1995). The Lau Basin is composed of three major active spreading ridges: the Central Lau Spreading Center (CLSC), the Eastern Lau Spreading Center (ELSC), and the southernmost part of the Valu Fa Ridge (VFR) south of 21°20'S (Jenner et al., 1987). The VFR extends for at least 165 km, is 5 to 6 km wide, with ridge flanks rising about 600 m above the surrounding seafloor (Taylor et al., 1996).

Since the early 1990s, a series of hydrothermal fields have been discovered along the VFR extensional zone (Fouquet et al., 1991a,b; 1993; Ishibashi et al., 2006; Reysenbach et al., 2006). According to Fouquet et al. (1993), two different volcanic and tectonic stages have been recognized from the southern and northern VFR. The Hine Hina hydrothermal field on the

Always consult and cite the final, published document. See http://www.minsocam.org or GeoscienceWorld

115 southern VFR is in a volcanic stage and is characterized by diffuse discharge (~40 ºC, Fouquet et
116 al., 1993; Lécuyer et al., 1999; Baker et al., 2005) through highly porous volcaniclastic material,
117 which results in the formation of extensive Fe-Mn-oxyhydroxide crusts covering sulfide deposits
118 within the volcanic material (Fouquet et al. 1993; Lécuyer et al., 1999; Fretzdorff et al., 2006).
119 The Vai Lili and Mariner fields have been found in the central VFR (Fouquet et al., 1991a,b;
120 Baker et al., 2005, 2006; Martinez et al., 2006) and are now in the volcanic/tectonic stage
121 (Fouquet et al., 1993). In these two fields, there are numerous black and white smokers
122 discharging fluids up to 400ºC in the Vai Lili and ~365ºC in the Mariner field (Takai et al., 2008).
123 Nonetheless, diffuse discharge of Fe-Si-Mn oxide is still occurring in this area (Lécuyer et al.,
124 1999). The White Church field in the northern VFR is in the tectonic stage and there is no
125 evidence for widespread Fe-Si-Mn oxide deposits there (Fouquet et al. 1993; Lécuyer et al., 1999)
126 except for the presence of a large number of barite chimneys and small Mn-oxide chimneys
127 controlled by major faults (Lécuyer et al., 1999). A new hydrothermal field at 176 º11′W, 20 º40′S
128 was discovered by Video Camera with deep tow at about 4 km south of the ABE hydrothermal
129 field in May 2007 during the expedition of R/V DaYang YiHao (Zhou et al., 2008). It was shown
130 that the newly discovered CDE hydrothermal field consists of at least 7 groups of chimneys
131 distributed along a deep tow transect from SW to NE for a length of more than 300 m at water
132 depths from 2199 to 2256 m (Fig. 1, Table 1). Significant amounts of anemones, crab, fish and
133 white microbial mats were associated with inactive chimneys in the hydrothermal field. Most of
134 the sulfides exist as pillars with a height ranging from < 1 m to > 5 m estimated from the length of
135 the rope with the deep tow camera. The largest chimney group had a height of about 12 m.

136 ## 3. Materials and Methods

137 Twelve samples were collected from ELSC and VFR of Lau Basin during the expedition of
138 R/V *DaYang YiHao* in May 2007. Sampling was performed in four hydrothermal fields: Samples
139 L9Y1, L9Y2 and L9Y3 came from the Mariner hydrothermal field; samples L81, L82 and L83
140 from the Vai Lili hydrothermal field; samples L5Y1, L5Y2, L6Y1 and L6Y2 from the Hine Hina
141 hydrothermal field; and l3Y1, 13Y2 and13Y3 from the newly discovered CDE hydrothermal field.
142 Sampling details and original sample descriptions are listed in Table 1. The samples were frozen
143 and stored at -20 °C prior to laboratory studies.

Always consult and cite the final, published document. See http://www.minsocam.org or GeoscienceWorld

The hydrothermal samples were impregnated with epoxy resin, carved and sectioned for petrographic observation and dehydrated by freeze drying. The dried samples were impregnated with a polyester resin mix under vacuum and 12 polished thin sections were made following the method of Camuti and McGuire (1999). The thin sections were then examined using a transmitted light microscope equipped with a Zeiss camera.

Mineralogical characterization of the hydrothermal Fe-Si samples included XRD, TG-DTA-DSC and FTIR analyses, all of which were made on powdered samples. Microstructural observations were carried out using a JEOL J 3M-840 scanning electron microscope (SEM) equipped with an energy dispersive energy spectrometer (EDS). The microscope was operated at a voltage of 10 keV and a range of beam currents of 18-22 mA.

XRD analysis was carried out using a PANalytical X'Pert system. Diffraction patterns in the 2.5-80° 2θ range were obtained in the step scan mode with a step of 0.02° 2θ and a counting time of 50 s per step. Operating conditions were 40 keV and 28 mA, using Cu$K\alpha$ radiation and a graphite monochromator. XRD analysis was performed after the sample was heated at RT, 200 °C, 450 °C, 600 °C, 800 °C and 1000 °C for 2 hours in an oxygen atmosphere.

Simultaneous TG-DTA-DSC analyses were carried out with a Netzsch STA 409 instrument, using ~50 mg of sample ground to <100 µm in an Al_2O_3 crucible in a dry air atmosphere with a flow rate of 80 mL/min. Al_2O_3 powder (Perkin-Elmer 0419-0197) was used as the standard. The experiment consisted of heating the sample from room temperature (RT) to 1200°C at a heating rate of 20°C/min.

The distribution of major and trace elements in the samples was determined by electron microprobe analysis (JEOL JXA-8100) at a 15 keV acceleration voltage, 35 nA current beam with a 1-2µm beam size. Prior to the analysis, a 10-20 nm thick carbon layer was splutter-coated on the samples. Standards used include synthetic oxide set (K_2O, Fe_2O_3, MnO_2, TiO_2, Cr_2O_3) for K, Fe and Mn, Ti, Cr, respectively; apatite for Ca and P; barite for Ba and S, olivine for Mg, Na, $SrSO_4$ for S. Counting times were 60 s.

FTIR spectra were recorded using a Nicolet 380 spectrometer. The spectra was recorded in the 4000 to 400cm^{-1} range and were collected after 256 scans at a resolution of 4 cm^{-1}. A KBr disc was used for sample preparation. The KBr (FTIR grade, Fluka) was dried at 200 °C for 24 h. To prepare KBr pellets, 1 mg of RM sample (derived from the RM-As (V) samples at pH 4, 7 and 10

Always consult and cite the final, published document. See http://www.minsocam.org or GeoscienceWorld

of the last point of isotherms, and coming from the extraction procedure steps of RM-As (V) samples at pH 4) was ground for 1-2 min together with 200 mg of KBr. The pellets were made using 90mg of the KBr-RM mixture. This mixture was then pressed in a die under vacuum for 4-6 min at 12t pressure to produce transparent disks about 1 mm thick and 13 mm in diameter. An empty KBr pellet was used as the reference and its spectrum was subtracted from the sample spectrum to suppress spectral artifacts caused by KBr impurities and water.

4. Results

4.1 XRD analysis

XRD results indicate the ubiquitous occurrence of amorphous opal-A and poorly crystalline Si-ferrihydritein in our samples. Minor amounts of halite (NaCl) and birnessite (δ-MnO_2) are also present. Opal-A is a common phase in the Lau Basin hydrothermal Fe-Si oxide precipitates. Its XRD pattern is characterized by a broad band at d = 4.0-4.1 Å, corresponding to a 2θ range of 17-26° centered at approximately 22.2°. Pure ferrihydrite is absent in all the samples. The dominant phase is Si-ferrihydrite characterized by a major broad band around d (110) = 3.0 Å (Fig. 2), which is shifted from that of pure ferrihydrite (ca. 2.54 Å; Karim 1984; Vempati and Loeppert 1989). In addition, the common 1.5 Å band (a double line with maxima at d(115) = 1.53 Å and d (300) = 1.48 Å) is poorly resolved (Carlson and Schwertmann, 1981) and can hardly be detected. This has been attributed to the incorporation of Si into the ferrihydrite structure (Vempati and Loeppert, 1989; Campbell et al., 2002).

4.2 Optical microscopy and SEM observations

Most of the Fe-Si oxide samples consist of a porous network of dendritic and filamentous structures which probably represent microbial growth forms (Fig. 3A-3D). The diameters of these filaments range from 5 to 10µm, and the lengths are commonly 30-500µm or even longer. In all the samples, the filaments constitute up to 40-70 vol% of the Fe-Si oxide precipitates. No other material was identified inside the mesh weaved by the filaments. In some samples, filament assemblages show vertically oriented fabrics, often originating from laminae or central points. A septate structure which could indicate the biogenic origin of the filaments was also identified in this Fe-Si sample which was very similar to that found in the previous studies (Little et al., 2004)

Always consult and cite the final, published document. See http://www.minsocam.org or GeoscienceWorld

(Fig. 3C). A proportion of the filaments have a distinctive twisted morphology. The branched filaments often recombine at intervals to form loose networks, most of which have a random orientation. In addition to the filaments, many spherules and larger amorphous aggregates were observed which were apparently contemporaneous with the filaments (Fig. 4).

SEM observations reveal an overwhelming presence of distinct bacterial forms as seen in Fig. 5. The filamentous, straight rod-like, short rod-like and twisted strands are commonly characterized by smooth surface. According to previous studies, the straight rod-like fragments are characteristic of *Leptothrix ochracea* (Kennedy et al., 2003a,c), while the distinctive helical structure is representative of the *Gallionella ferruginea* stalk (Hallbeck and Pederson, 1991). Oval and spherical features also occur in some samples. The spheres often have small diameters ranging from 0.1-1μm and encrust the precursor filaments. Most features of these microbes are hidden under the small sphere that has encrusted them. Major elements detected by EDS (Fig. 6) on the surface of the filaments include Fe, Si, P, Na, Cl and O but the small sphere contains only Si and O, indicating that it consists only of pure opal-A.

4.3 Thermal analysis（TG -DTG-DSC）

As shown in the TG-DTG curves (Fig. 7), two sharp mass loss events occurred at 25-260°C and 800-1030°C, which correspond to the endothermic peaks at 106-138 °C and 918-968 °C, respectively, on the DTG curves. The mass loss corresponding to the first endothermic peak accounts for 6.3-11.2 wt%, whereas the second endothermic accounts for 5.0-8.4 wt%. Overall, the total mass loss of all three studied samples is within the range of 19.9~24.3 wt% (Fig. 7), which mainly result from dehydration of two types of water present in Fe-Si oxides, i.e., the isolated non-hydrogen bonded molecules and hydroxyl groups trapped in the structure as fluid inclusions, and the strongly hydrogen-bonded accumulations of water molecules or hydroxyls either within the structure or on external and internal surfaces. The DSC curves are consistent with the TG-DTG results with an endothermic peak at about 110-140°C and a broader endothermic peak at 800-1050°C. The most striking feature of the DSC curves is the absence of the sharp peaks. The moderate endothermic peaks at 408°C and 558°C of sample L9Y3 can probably be attributed to the presence of birnessite, which starts to transform to well-crystallized phases at 400-600°C when heated in air (Golden, et al., 1986). According to the mass losses shown in TG curves (Fig.

Always consult and cite the final, published document. See http://www.minsocam.org or GeoscienceWorld

7), the endothermic peak at ca. 106-138°C can be attributed to the loss of absorbed water and the endothermic peak at 918-968°C to dehydroxylation.

To further investigate the thermal process, we carried out XRD after a series of stepwise heating of the Fe-Si oxide sample (Fig. 8). No obvious transformation could be observed below 600 °C. The presence of hematite is commonly observed at ca. 800 °C with its maximum at 1000 °C. In addition, Opal-A begins to transform to opal-CT at ca. 800°C and shows increasing degrees of crystallinity. When heated to 1000°C, Fe-oxyhydroxide completely transforms to hematite and the opal-CT to cristobalite.

4.4 FTIR

FTIR was used to characterize the water and hydroxyl groups as well as chemical bonds in the structures of Fe-Si oxides. All the analyzed samples display similar FTIR spectral features, which are summarized in Table 2. Infrared absorption spectra (Fig. 9) display distinct features at 3390-3440 cm^{-1} and ca.1640 cm^{-1} which which can be assigned to the stretching vibration of –OH and to the bending vibration of water absorbed, respectively (Koji and Solomon, 1977).

The asymmetric Si-O stretching mode at 1002-1108 cm^{-1} is derived from the vibrations of SiO_4 tetrahedra with three or four bridge oxygens (Lazarev, 1972; Farmer, 1974). The obvious shift of the band from about 1000 cm^{-1} (1002 cm^{-1} for L6Y1 and 1010 cm^{-1} for L5Y2) to higher wave numbers (1103 cm^{-1} for L13Y1 and 1108 cm^{-1} for L9Y2) may reflect the presence of unpolymerized, partially unpolymerized up to fully polymerized silica (Carlson and Schwertmann, 1981). A medium intensity band at 942 cm^{-1} can be assigned to the Si-O-Fe stretching (Carlson and Schwertmann, 1981). The 786 cm^{-1} band is assigned to the Si-O stretching of the SiO_4 ring structure. This is usually correlated with fully condensed Si atoms surrounded by four Si-O-Si linkages (Landmesser et al., 1997). The absorption bands around 647 cm^{-1} and 470 cm^{-1} may result from the stretching vibration of Fe-O (Vempati and Loeppert, 1989; Ying et al., 2007), suggesting the presence of ferrihydrite (Vempati et al., 1990).

4.5 EMPA

Two types of Fe-Si oxides were identified by Electron Microprobe Analysis. Type I is rich in Fe with an average content up to 44.33 wt % (Fe_2O_3). This type of Fe-Si oxide corresponds to

Always consult and cite the final, published document. See http://www.minsocam.org or GeoscienceWorld

Si-ferrihydrite with d(110) ≈ 3.0 Å. Minor Fe was found in the type II Fe-Si oxide with the Fe_2O_3 content ranging from 0.15 to 6.60 wt%. This type corresponds to the opal-A identified by XRD with d(110) = ca. 2.5 Å. Type I Fe-Si oxide has a Si content between 30.31-66.01 wt% (mean 46.67 wt % SiO_2) with a Si:Fe molar ratio of 0.72-3.08 (mean 1.51). By contrast, type II Fe-Si oxide contains a much higher Si content, up to 66.8-88.5 wt% (mean 83.1 wt% SiO_2) with the Si:Fe molar ratio of 16.7-785 (mean 207.5). However, other elements such as P, Ca, Mg and Na show higher contents in the type I sample, indicating these elements are more associated with Si-ferrihydrite. The higher P content may possibly be attributed to the adsorption of phosphor on Fe oxide surface (Konhauser et al., 2007). One analysis point in the type II sample has the highest Al content (up to 12.63 wt %), which may be due to occasional addition of volcanic fragments.

It is noted that the EPMA totals are significantly smaller than 100%, ranging from 86.2 to 96.4 wt%. This is probably due to evaporation of water from the samples under electron beam irradiation. However, the water contents of the samples (19.9-24.3 wt%), are much larger than those deduced from the EMPA analysis (3.6-13.8 wt%), suggesting partial water evaporation.

5 Discussions

5.1 Precipitation of Fe oxides in modern hydrothermal vents

Microbial activity is commonly involved in Fe-Si oxide formation in modern hydrothermal vents (e.g., Emerson and Moyer, 2002, Emerson et al.,2007; Kennedy et al., 2003a,b,c; Chan et al., 2009; Kato et al., 2009 ; Langley et al., 2009 ; Edwards et al., 2011). In this study, we have observed many variants of stalks, sheaths and other mineralized structures generally attributed to *Gallionella ferruginea*, *Leptothrix ochracea* and *Mariprofundus ferrooxydans*. Based on the SEM and light microscopic results, we infer that the microbial Fe oxide occurs as a mass of filaments which often combine together to form a loose network. These networks are characterized by high porosities, and fluids can migrate through them relatively freely. The neutrophilic Fe-oxidizing bacteria use energy from Fe^{2+} oxidation to fix CO_2, a metabolic process which leads to the deposition of ferrihydrite (Emerson, 2000; Kennedy 2003a). As a result, the electronegative surfaces of the cells and extracellular polymers which contain functional groups (such as carboxyl and phosphate) play an important role in the Fe oxide formation. The groups themselves are

Always consult and cite the final, published document. See http://www.minsocam.org or GeoscienceWorld

highly reactive and can bind Fe^{2+} when the reduced acidic fluids are discharged into an oxidizing neutral environment. Microbial cell surfaces are also effective adsorbents of pre-existing nano- and micro-sized iron oxide phases (Langley et al., 2009). The initially precipitated iron can also act as a catalyst for the accelerated auto-catalytic hydrothermal deposition of Fe-oxyhydroxides (Boyd and Scott, 2001). Biogenetic Fe-oxyhydroxide therefore precipitates on the surface of cells and forms filaments at the stage when hydrothermal fluids can mix freely with seawater.

However, the precipitation mechanism of Fe in hydrothermal vent is fairly complex. A challenge is how to evaluate the exact role of biotic vs. abiotic precipitation in the formation of Fe-Si oxides. These phases generally precipitate at an oxic–anoxic interface where the rapid rate of abiotic Fe(II) oxidation coupled with oxygen reduction can outpace biotic oxidation in iron microbial mats (James and Ferris, 2004; Druschel et al., 2008). Nonetheless, competition between the kinetics of microbial and abiotic oxidation has not been established. The observation of many spherules and larger amorphous aggregates in our samples may provide an important clue in the explanation of this mechanism. The presence of amorphous aggregates in particular is a strong indication that abiogenic precipitation plays an important role in the Fe-oxyhydroxide formation, supporting the conclusion of Boyd and Scott (2001) that amorphous Fe-oxyhydroxides precipitate hydrothermally as abiogenic products. However, it is difficult to estimate the relative proportions of abiogenic and bacteriogenic Fe oxide precipitation from our observations as metabolic activity of even small colonies of Fe oxidizing bacteria may alter the local physiochemical conditions to increase the precipitation of Fe oxides more than would occur by abiogenic processes alone (Emerson and Moyer 2002; Kennedy et al., 2003a,b,c). To resolve this issue, quantitative experiments using living Fe oxidizing bacteria need to be performed.

5.2 Silicification pattern of the mat

Our EMPA analyses show that silica has the highest concentrations in Fe-Si oxide mats, indicating that silica precipitation (mainly opal-A) ultimately dominates during the hydrothermal Fe-Si oxide formation. As stated earlier, variants of filaments coated with ferrihydrite gradually weave together to form a loose network whereas silica precipitates inside the network during the first growth stage. It can therefore be hypothesized that the precipitation of silica onto the surface of the ferrihydrite encrustation or into the porous network will lead to a continuing decrease in the

Always consult and cite the final, published document. See http://www.minsocam.org or GeoscienceWorld

316 porosity of the filament network. As a result, mixing between seawater and hydrothermal fluid
317 will be restricted or even end. In other words, once silica starts to precipitate, there is no niche
318 inside the mat for Fe-oxidizing bacteria to live, and the biomineralization of the Fe declines
319 accordingly.

320 There are at least two chemically distinct processes involved in H_4SiO_4 association with
321 ferrihydrite and the importance of each process depends on the amount of H_4SiO_4 present at the
322 ferrihydrite surface, i.e. the molar ratio of Si:Fe in the ferrihydrite. When the Si: Fe ratio is low
323 ($<$ 0.05), H_4SiO_4 appears to be associated with monomeric silica (Swedlund and Webster, 1999).
324 However, when the Si:Fe ratio is increased to 0.05-0.2, the H_4SiO_4 is associated with ferrihydrite
325 via a siloxane linkage (Si-O-Si), essentially resulting in polymerization to form a separate silica
326 phase (Swedlund and Webster, 1999). In fluids supersaturated with amorphous silica, hydroxyl
327 groups on the silicic acid molecule combine to form siloxane bonds, resulting in spontaneous
328 polymerization of monomeric Si to form polymeric Si clusters and three-dimensional
329 nanoparticles 1-2 nm in diameter (Iler, 1979). Our FTIR results show that the Si-O-Si bond
330 indicative of [SiO_4] polymerization is very common. Moreover, the Si:Fe molar ratios of all the
331 Fe-Si oxide samples are greater than 0.2, indicating the dominant role of fully polymerized silica
332 in the mat silicification. However, unpolymerized silica or partially polymerized silica still exists
333 in the natural Fe-Si oxide. For instance, the band at 942cm^{-1} in sample L13 is indicative of a
334 Fe-O-Si bond and is a consequence of binding Si to Fe-OH functional groups on the ferrihydrite
335 surface. Furthermore, the band at 942 cm^{-1} rather than at 925-935cm^{-1} for unpolymerized Si can
336 hardly be due to a contribution from the band at ca. 1100cm^{-1} for fully polymerized silica. The
337 position of the band therefore suggests that, in addition to unpolymerized Si, partially polymerized
338 Si is also present. Thus silicification of the mat is probably a multistage and dynamic process. To
339 summarize, the silicification process may correspond to a distinct stage when mixing between
340 hydrothermal fluid and seawater is relatively free, the solution is undersaturated with respect to
341 amorphous silica and the Si bound to Fe-OH functional groups at the surface and form the
342 unpolymerized silica. The decrease in the porosity in the filament network leads to gradual
343 restriction of the mixing between seawater and the hydrothermal fluid. Consequently, the solution
344 become supersaturated with respect to amorphous silica as a result of the conductive cooling and

Always consult and cite the final, published document. See http://www.minsocam.org or GeoscienceWorld

initiates spontaneous Si polymerization. The presence of the highly intense Si-O-Si bond at 786 cm^{-1} indicates that the inorganic polymerization reaction is most important in the Fe-Si oxide precipitation. This study therefore demonstrates that ferrihydrite filaments form by neutral Fe oxidizing bacteria and display a strong affinity for Si and can readily accumulate silica from hydrothermal fluids. Monomeric species can bind directly onto ferrihydrite surface sites and form stable surface complexes. In addition, at high Si concentrations, the ferrihydrite surfaces can act as a template for silica polymerization (Carlson and Schwertmann, 1981; Swedlund and Webster, 1999; Yee et al., 2003). Moreover, biomineralization process of the mats has been investigated in modern hydrothermal vent systems (Juniper and Fouquet., 1988; Toner et al., 2009; Peng et al., 2010; Edwards et al., 2011). In a recent study of Fe-Si deposits from the Edmond hydrothermal vent, Peng et al. (2010) demonstrated that cells are commonly enclosed in a matrix of amorphous silica, whereas acicular Fe oxide precipitates intracellularly in the cytoplasm inside the cell and extracellularly on the surfaces of cell wall and silica matrix.

5.3 Thermal stability and implications of hydrothermal Fe-Si oxide deposition

Ferrihydrite is a metastable phase and eventually transforms to more stable iron oxides, such as goethite, lepidocrocite and/or hematite (Boyd and Scott, 1999; Langley et al., 2009; Parenteau and Cady, 2010). Similarly, the water-bearing opal-A progressively transforms to opal-CT/C or even microcrystalline quartz with the polymorphs showing increasing degrees of structural order and crystallinity (Lee, Garcia-Valles et al., 2008). However, transformations and diagenesis of Fe-Si oxide precipitates in modern hydrothermal vents are limited. Most Fe-Si oxides still occur as Fe-bearing opal-A or Si-ferrihydrite. Our thermal analysis results reveal that after the first dehydration of trapped/absorbed water between 25 and 260°C, the Fe-Si oxide can remain stable up to 800 °C, at which it transforms to hematite while silica to opal-CT. This transformation ultimately ends at ca. 970 °C, reflecting the high thermal stability of the modern hydrothermal Fe-Si oxide precipitate.

According to Carlson and Schwertmann (1981), a simple mixture of pure ferrihydrite and amorphous silica does not promote thermal stability of both minerals. This probably reflects the presence of microbial cells and detrital organic material, as described by Kennedy et al. (2004). These authors hypothesized that the binding of ferric iron and nucleation of ferrihydrite to

Always consult and cite the final, published document. See http://www.minsocam.org or GeoscienceWorld

374 bacterial surface functional groups (i.e., carboxyl and phosphoryl groups) would constrain the
375 rotation of the nanoparticles, thereby inhibiting subsequent aggregation and crystal growth
376 (Banfield et al. 2000). However, the amount of organic material in Fe-Si oxide is very low (< 0.1
377 wt%, unpublished data) because of rapid decomposition of the organic matter (cells and
378 extracellular polymeric substance (EPS)) when exposed to oxygenic seawater after its death or due
379 to mineralization (such as silicification) which occurs while the cell is still alive (Guidry and
380 Chafetz, 2003; Konhauser et al., 2004). In fact, several studies have shown that most Fe-Si oxide
381 precipitates (especially silica sinters) do not usually contain residual organic matter (e.g.,
382 Konhauser et al., 2004; Hofmann et al., 2008). Moreover, inorganic polymerized silica dominates
383 the volume in the Fe-Si oxide precipitates in our samples. The inhibitory effect of functional
384 groups on the surface of the organism is a minor factor in retarding the transformation of Fe-Si
385 oxide.

386 Considerably higher temperatures are needed for the thermal conversion of ferrihydrite to
387 hematite if ferrihydrite contains foreign elements such as Si, P, Al. Previous DTA experiments
388 show that an increase in the Si/(Si+Fe) ratio from 0 to 0.153 in the synthetic 2-line ferrihydrite
389 produced by coprecipitation can shift the exothermic peak from 331 to 778 °C while reducing its
390 intensity significantly (Carlson and Schwertmann, 1981, Campbell et al. 2002). Similarly, a 2-line
391 ferrihydrite with a Si/(Si+Fe) ratio of 0.11 remained essentially unchanged after being heated to
392 600 °C but was completely converted to hematite at 850 °C (Glasauer et al. 2000). As mentioned
393 above, several authors have attributed the high thermal stability of Si-rich ferrihydrite to the
394 surface effects of Si such as the formation of Si-O-Fe bonds that hinder the dehydroxylation and
395 subsequent atomic rearrangement to hematite (Zhao et al., 1994; Cismasu et al., 2011). However,
396 another possibility is that Si substitution increases the stability of ferrihydrite. For example,
397 Vempati et al. (1990) postulate that Si forms a structured bond (Si-O-Fe) in ferrihydrite based on
398 X-ray photoelectron spectroscopy (XPS) data. Unit cell measurements (XRD) of Si-containing
399 hematite heated to 672 °C in a DTA instrument show that *a* and *c* increase as the Si/(Si+Fe) ratio
400 increases from 0 to 0.07, indicating that small amounts of Si are incorporated into the structure,
401 probably compensating for the Fe(III) deficiency (Campbell et al. 2002). All the results described
402 above are based on studies of synthetic ferrihydrite.

403 Our studies show that natural Fe-Si oxide samples from modern hydrothermal vents behave

Always consult and cite the final, published document. See http://www.minsocam.org or GeoscienceWorld

similarly up to the conversion temperature, 970 °C. Although the ferrihyrite-hematite transformation has not been fully understood, the incorporation of Si into the structure appears to lead to its higher thermal stability. The hydrothermal fluid in the Mariner field has a Si:Fe ratio of 1.19-1.41, whereas the Si:Fe ratio for the fluid in the southward Vai Lili field can be as high as 7.86 (average value, Takai et al., 2008). This implies that significant Si may be incorporated into the ferrihydrite structure or adsorb on the ferrihydrite surface. In order for Si-ferrihydrite to transform to hematite, Fe-O-Si bonds must be broken prior to the formation of Fe-O-Fe bonds. With an increasing concentration of Si, higher temperatures are needed for the ferrihydrite-hematite transformation. For instance, previous study has shown that synthetic Si-ferrihydrite does not transform to hematite below 800 °C (Campbell et al. 2002), which is also in accordance with our result. Furthermore, the presence of slightly abundant P (mean content 1.01wt% for type I Fe-Si oxide) is also expected to increase the transformation temperature (Quin et al., 1988; Zachara et al., 2011).

Most evidences suggest that chemical components of BIF were sourced from hydrothermal systems that contained abundant Fe and SiO_2 (Morris 1993). Moreover, it is generally accepted that microbes played a significant role in the formation of ancient BIFs (Cloud, 1965; Brown et al., 1995; Konhauser et al., 2002, 2011; Posth et al., 2008; Parenteau and Cady, 2010; Li et al., 2011). Our results thus have some implications to the formation process of BIFs. Most of our samples from the modern hydrothermal vent system consist of a natural intermixture of Si-ferrihydrite and opal-A rather than a single mineral. Then it can be assumed that, in the presence of saturated silica, biogenic Fe oxide cannot precipitate separately because of the binding effect of biogenic Fe oxide on dissolved silica. According to the commonly accepted temperature of the Archean Ocean (10-85°C, Posth et al., 2008), the occurrence of segregated crystalline Fe and Si oxides is impossible. Primary alternating Si- and Fe-rich layers were therefore absent in the Archean ocean, even at a micro-meter scale. A plausible explanation for the alternating BIF deposits is the later diagenetic maturation of Fe-Si oxides that can separate into pure crystalline silica and iron oxides in an oxygenated environment. Following with the relatively abundant water (19.9~24.3 wt%, according to our thermal analysis result) escaping from the Fe-Si deposits during digenetic process, the Si-rich thin band alternated with the Fe-rich thin band was possibly expected to form. Although this hypothesis still needs further work to support because the real condition that the

Always consult and cite the final, published document. See http://www.minsocam.org or GeoscienceWorld

Fe-Si oxide deposits has experienced during an extreme long period might outrun our imagination, the findings presented here at least provide another different perspective to reconsider the continuing BIF enigma.

Acknowledgements

This study was supported by the Natural Science Foundation of China (Project No. 40976045, 40976025 and 40976036). We gratefully thank Professor Fuya Wang from the Guangzhou Institute of Geochemistry, Chinese Academy of Sciences (GIGCAS), for his help in XRD analysis and Professor Peng Yuan from GIGCAS for their help in thermal analysis. We also thank Wei Huang from Qingdao Institute of Marine Geology for his help in drawing Fig. 1 and three anonymous reviewers for their constructive suggestions.

References

Baker, E. T., Resing, J. A., Walker, S. L., Martinez, F., Taylor, B. and Nakamura, K. (2006) Abundant hydrothermal venting along melt-rich and melt-free ridge segments in the Lau back-arc basin. Geophysical Reseach Letters, 33, L07308, doi:10.1029/2005GL025283.

Baker, E.T., Massoth, G.J., Nakamura, K., Embley, R.W., de Ronde, C.E.J., and Arculus, R.J. (2005) Hydrothermal activity on near-arc sections of back-arc ridges: Results from the Mariana Trough and Lau Basin, Geochemistry, Geophysics, Geosystems, 6, Q09001, doi:10.1029/2005GC000948.

Banfield, J.F., Welch, S.A., Zhang, H., Ebert, T.T., and Penn, R.L. (2000) Aggregation-based crystal growth and microstructure development in natural iron oxyhydroxide biomineralization products. Science, 289, 751–754.

Bevis, M., Taylor, F.W., Schutz, B.E., Recy, J., Isacks, B.L., Hely, S., Singh, R., Kendrick, E., Stowell, J., Taylor, B., and Calmant, S. (1995) Geodetic observations of very rapid convergence and backarc extension at the Tonga arc, Nature, 374, 249–251.

Boyd, T.D, and Scott, S.D. (1999) Two-XRD-line ferrihydrite and Fe-Si-Mn oxyhydroxide mineralization from Franklin Seamount, western Woodlark Basin, Papua New Guinea, Canadian Mineralogist, 37, 973–990.

Boyd, T.D., and Scott S.D. (2001) Microbial and hydrothermal aspects of ferric oxyhydroxides and ferrosic hydroxides: the example of Franklin Seamount,Western Woodlark Basin, Papua

Always consult and cite the final, published document. See http://www.minsocam.org or GeoscienceWorld

New Guinea. Geochemical Transactions 2, 45 (5 September 2001).

Brown, D.A., Gross, G.A., and Sawicki, J.A. (1995) A review of the microbial geochemeistry of banded iron-formations. The Canadian Mineralogist, 33, 1321–1333.

Campbell, A. S., Schwertmann, U., Stanjek, H., Friedl, J., Kyek, A., and Campbell, P. A. (2002) Si incorporation into hematite by heating Si-ferrihydrite. Langmuir, 18, 7804–7809.

Camuti, K.S., and McGuire, P.T. (1999) Preparation of polished thin sections from poorly consolidated regolith and sediment materials. Sedimentary Geology, 128, 171–178.

Carlson, L., and Schwertmann, U. (1981) Natural ferrihydrites in surface deposits from Finland and their association with silica. Geochimica et Cosmochimica Acta, 45, 421–429.

Chan, C.S., Fakra, S.C., Edwards, D.C., Emerson, D. and Banfield, J.F. (2009) Iron oxyhydroxide mineralization on microbial extracellular polysaccharides. Geochimica et Cosmochimica Acta, 73, 3807–3818.

Childs, C.W., Kanasaki, N. and Yoshinaga, N. (1993) Effect of Heating in Air on Si- and Ge-containing Ferrihydrites. Clay Science, 9, 65–80.

Cismasu, A.C., Michel, F.M., Tcaciuc, A.P., Tyliszczak, T., and Brown Jr., G.E. (2011) Composition and structural aspects of naturally occurring ferrihydrite. Comptes Rendus Geoscience, 343, 210–218.

Cloud, P.E., Jr. (1965) Significance of the Gunflint (Precambrian) microflora. Science, 148, 27–35.

Corliss, J.B., Dymond, J., Gordon, L.I., Edmond, J.M., von Herzen, R.P., Ballard, R.D., Green, K., Williams, D., Bainbridge, A., Grane, K., van Andel, T.H., 1979. Submarine Thermal Springs on the Galápagos Rift. Science 203,1073–1083.

Davis, R., and Moyer, C. (2008) Extreme spatial and temporal variability of hydrothermal microbial mat communities along the Mariana island arc and southern Mariana backarc system. Journal of Geophysical Research 113, B08S15. doi:10.1029/2007JB005413.

Druschel, G., Emerson, D., Sutka, R., Suchecki, P. and Luther, G.W. (2008) Low-oxygen and chemical kinetic constraints on the geochemical niche of neutrophilic iron(II) oxidizing microorganisms. Geochimica et Cosmochimica Acta, 72, 3358–3370.

Edwards, K.J. (2004) Formation and degradation of seafloor hydrothermal sulfide deposits. In: Amend, J.P., Edwards, K.J., Lyons, T.W. (Eds.), Biogeochemistry of Sulfur-Past and Present.

Always consult and cite the final, published document. See http://www.minsocam.org or GeoscienceWorld

Geological Society of America Special Papers, pp. 83–96.

Edwards, K.J., Glazer, B.T., Rouxel, O.J., Bach, W., Emerson, D., Davis, R.E., Toner, B.M., Chan, C.S., Tebo, B.M., Staudigel, H. and Moyer, C.L. (2011) Ultra-diffuse hydrothermal venting supports Fe-oxidizing bacteria and massive umber deposition at 5000m off Hawaii. The ISME Journal, doi:10.1038/ismej.2011.48.

Edwards, K.J., McCollom, T.M., Konishi, H., and Buseck, P.R. (2003) Seafloor bioalteration of sulfide minerals: Results from in situ incubation studies. Geochimica et Cosmochimica Acta, 67, 2843–2856.

Eggleton, R.A. and Fitzpatrick, R.W. (1988) New data and a revised structural model for ferrihydrite. Clays and Clay minerals 36, 111–124.

Emerson, D., (2000) Microbial oxidation of Fe(II) and Mn(II) at circumneutral pH. In: Lovely, D.R. (Ed.), Environmental Microbe–Metal Interactions. ASM press, Washington, DC, pp. 31–52.

Emerson, D., Moyer, CL. (2002) Neutrophilic Fe-oxidizing bacteria are abundant at the Loihi Seamount hydrothermal vents and play a major role in Fe oxide deposition. Applied and environmental microbiology, 68, 3085–3093.

Emerson. D., Rentz, J.A., Lilburn, T.G., Davis, R.E., Aldrich, H., Chan, C., and Moyer, C.L. (2007) A novel lineage of proteobacteria involved in formation of marine Fe-oxidizing microbial mat communities. PloS one, 2(7): e667, doi: 10.1371/journal.pone.0000667.

Farmer, V.C. 1974. The layer silicates: Ch 15. In Infrared Spectra of Minerals. Farmer, V. C. ed. London: Mineralogical Society, 331–363.

Fein, J.B., Scott, S., and Rivera, N. (2002) The effect of Fe on Si adsorption by Bacillus subtilis cell walls: insights into non-metabolic bacterial precipitation of silicate minerals. Chemical Geology, 182, 265–273.

Fouquet Y., von Stackelberg U ., Charlou J.L., Donval J.P., Foucher J.P., Erzinger J., Herzig P., Mühe R., Wiedicke M., Soakai S., and Whitechurch H. (1991a) Hydrothermal activity in the Lau back-arc basin: Sulfides and water chemistry. Geology, 19, 303–306.

Fouquet Y., Von Stackelberg U., Charlou J.L., Donval J.P., Erzinger J., Foucher J.P., Herzig P., Mühe R., Soakai S., Wiedicke M. and Whitechurch H. and (1991b) Hydrothermal activity and metallogenesis in the Lau back-arc basin. Nature, 349, 778–781.

Always consult and cite the final, published document. See http://www.minsocam.org or GeoscienceWorld

523 Fouquet,Y., von Stackelberg, U., Charlou, J.L., Erzinger, J., Herzig, P.M. Muehe, R., and
524 Wiedicke, M. (1993) Metallogenesis in back-arc environments: the Lau Basin example.
525 Economic Geology, 88, 2154–2181.
526 Fretzdorff, S., Schwarz-Schampera, U., Gibson, H.L., Garbe-Schönberg, C.-D., Hauff, F., and
527 Stoffers, P. (2006) Hydrothermal activity and magma genesis along a propagating back-arc
528 basin: Valu Fa Ridge (southern Lau Basin). Journal of Geophysical Research, 111, B08205,
529 doi:10.1029/2005JB003967.
530 García-Ruiz, J.M., Carnerup, A., Christy, A.G., Welham, N.J., and Hyde, S.T. (2002) Morphology:
531 an ambiguous indicator of biogenicity. Astrobiology, 2, 353–369.
532 García-Ruiz, J.M., Hyde, S.T., Carnerup, A.M., Christy, A.G., Van Kranendonk, M.J., and Welham,
533 N.J. (2003) Self-assembled silica-carbonate structures and detection of ancient microfossils.
534 Science, 302, 1194–1197.
535 Garcia-Valles, M., Fernandez-Turiel, J.L., Gimeno-Torrente, D., Saavedra-Alonso, J., and
536 Martinez-Manent, S. (2008) Mineralogical characterization of silica sinters from the El Tatio
537 geothermal field, Chile. American Mineralogist, 93, 1373–1383.
538 Glasauer, S.M., Hug, P., Weidler, P.G., and Gehring, A.U. (2000) Inhibition of sintering by Si
539 during the conversion of Si-rich ferrihydrite to hematite. Clay and Clay minerals, 48, 51–56.
540 Golden, D.C., Dixon, J.B., and Chen, C.C. (1986) Ion exchange, thermal transformations, and
541 oxidizing properties of birnessite. Clays and Clay minerals, 34, 511–520.
542 Guidry, S.A. and Chafetz, H.S. (2003) Siliceous shrubs in hot springs from Yellowstone National
543 Park, Wyoming, U.S.A. Canadian Journal of Earth Sciences, 40, 1571–1583.
544 Hallbeck, L., and Pedersen, K. (1991) Autotrophic and mixotrophic growth of *Gallionella*
545 *ferruginea.* Journal of General Microbiology, 137, 2657–2661.
546 Hawkins, J.W. (1995) Evolution of the Lau Basin: Insights from ODP Leg 135. In: Taylor, B.,
547 Natland, J. (Eds.), Active Margins and Marginal Basins of the Western Pacific. AGU
548 Geophysical Monograph 88, pp. 125–173.
549 Hekinian, R., Hoffert, M., Laroqué, P., Cheminée, J.L., Stoffers, P., and Bideau, D. (1993)
550 Hydrothermal Fe and Si oxyhydroxide deposits from South Pacific intraplate volcanoes and
551 East Pacific Rise axial and off-axial regions. Economic Geology, 88, 2099–2121.
552 Herzig P.M., Becker K.P., Stoffers P., and Bäcker H. (1988) Hydrothermal silica chimney fields in

Always consult and cite the final, published document. See http://www.minsocam.org or GeoscienceWorld

the Galapagos Spreading Center at 86 °W. Earth and Planetary Science Letters, 89, 261–272.

Hodges, W., and Olson, J.B. (2009) Molecular comparison of bacterial communities within iron-containing flocculent mats associated with submarine volcanoes along the Kermadec Arc. Applied and environmental microbiology, 75, 1650–1657.

Hofmann, B.A., Farmer, J.D., Von Blanckenburg, F., and Fallick, A. (2008) Subsurface filamentous fabrics: an evaluation of origins based on morphological and geochemical criteria, with implications for exopaleontology. Astrobiology 8, 87–117.

Hopkinson, L., Roberts, S., Herrington, R., and Wilkinson, J. (1998) Self-organization of submarine hydrothermal siliceous deposits: Evidence from the TAG hydrothermal mound, 26ºN Mid-Atlantic Ridge. Geology, 26, 347–350.

Iler, R.K. (1979) The chemistry of silica: solubility, polymerization, colloid and surface properties, and biochemistry. Wiley, New York.

Ishibashi, J., Lupton, J.E., Yamaguchi, T., Querellou, J., Nunoura, T., Takai, K. (2006) Expedition reveals changes in Lau Basin hydrothermal system. Eos, Transactions, American Geophysical Union, 87, 13–17.

Jambor, J.l. and Dutrizac, J.E. (1998) Occurrence and constitution of natural and synthetic ferrihydrite, a widespread iron oxyhydroxide. Chemical reviews, 98, 2549–2585.

James, R.E., and Ferris, F.G. (2004) Evidence for microbial-mediated iron oxidation at a neutrophilic groundwater spring. Chemical Geology, 212, 301–311.

Jenner, G.A., Cawood, P.A., Rautenschlein, M., and White, W.M. (1987) Composition of back-arc basin volcanics, Valu Fa Ridge, Lau Basin: evidence for a slab-derived component in their mantle source, Journal of Volcanology and Geothermal Research, 32, 209–222.

Jones, B. and Renaut, R.W. (2004) Water content of opal-A: implications for the origin of laminae in geyserite and sinter: Journal of Sedimentary Research, 74, 117–128.

Juniper, S.K., and Fouquet, Y. (1988) Filamentous iron-silica deposits from modern and ancient hydrothermal site: Canadian Mineralogist 26, 859–869.

Karim, Z. (1984) Characteristics of ferrihydrites formed by oxidation of $FeCl_2$ solutions containing different amounts of silica. Clay and Clay Minerals, 32, 181–184.

Kato, S., Kobayashi, C., Kakegawa, T., and Yamagishi, A. (2009) Microbial communities in iron-silica-rich microbial mats at deep-sea hydrothermal fields of the Southern Mariana

Always consult and cite the final, published document. See http://www.minsocam.org or GeoscienceWorld

583 Trough. Environmental Microbiology, 11, 2094–2111.
584 Kennedy C.B., Scott S.D., and Ferris F.G. (2004) Hydrothermal phase stabilization of 2-line
585 ferrihydrite by bacteria, Chemical Geology, 212, 269–277.
586 Kennedy, C.B., Martinez, R.E., Scott, S.D., and Ferris, F.G. (2003b) Surface chemistry and
587 reactivity of bacteriogenic iron oxides from Axial Volcano, Juan de Fuca Ridge, north-east
588 Pacific Ocean. Geobiology, 1, 59–69.
589 Kennedy, C.B., Scott, S.D. and Ferris, F.G. (2003c) Ultrastructure and potential sub-seafloor
590 evidence of bacteriogenic iron oxides from Axial Volcano, Juan de Fuca Ridge, north-east
591 Pacific Ocean. FEMS Microbiology Ecology, 43, 247–254.
592 Kennedy, C.B., Scott, S.D., and Ferris, F.G. (2003a) Characterization of bacteriogenic iron oxide
593 deposits from Axial Volcano, Juan de Fuca Ridge, north-east Pacific Ocean.
594 Geomicrobiology Journal, 20, 199–214.
595 Koji, N., and Solomon, P.H. (1977) Infrared adsorption spectroscopy. San Francisco: Holden-Day.
596 Inc.
597 Konhauser, K.O., Hamade, T., Raiswell, R., Morris, R.C., Ferris, F.G., Southam, G., and Canfield,
598 D.E. (2002) Could bacteria have formed the Precambrian banded iron formations? Geology,
599 30, 1079–1082.
600 Konhauser, K.O., Jones, B., Phoenix, V.R., Ferris, G. and Renaut, R.W. (2004) The microbial role
601 in hot spring silicification. Ambio, 33, 552–558.
602 Konhauser, K.O., Kappler, A., and Roden, E.E. (2011) Iron in microbial metabolisms. Elements, 7,
603 89–93.
604 Konhauser, K.O., Lalonde, S.V., Amskold, L., and Holland, H.D. (2007) Was There Really an
605 Archean Phosphate Crisis? Science, 315, 1234.
606 Kristall, B., Kelly, D.S. Hanington, M.D., and Delaney, J.R. (2006) Growth history of a diffusely
607 venting sulfide structure from the Juan de Fuca Ridge: A petrological and geochemical study.
608 Geochemistry, Geophysics, Geosystems, 7, Q07001, doi:10.1029/2005GC001166.
609 Landmesser, H., Kosslick, H., Storek, W., and Fricke, R. (1997) Interior surface hydroxyl groups
610 in ordered mesoporous silicates. Solid State Ionics, 271, 101–103.
611 Langley S, Igric P, Takahashi Y, Sakai Y, Fortin D, Hannington MD, and Schwarz-Schampera U.
612 (2009) Preliminary characterization and biological reduction of putative biogenic iron oxides

Always consult and cite the final, published document. See http://www.minsocam.org or GeoscienceWorld

(BIOS) from the Tonga-Kermadec Arc, southwest Pacific Ocean. Geobiology, 7, 35–49.

Lazarev, A. N. (1972) Vibrational Spectra and Structure of Silicates. New York: Plenum Press, 123–124.

Lécuyer, C., Dubois, M., Marignac, C., Gruau, G., Fouquet, Y., and Ramboz, C. (1999) Phase separation and fluid mixing in subseafioor back arc hydrothermal systems: A microthermometric and oxygen isotope study of fluid inclusions in the barite-sulfide chimneys of the Lau basin. Jornal of Geophysical Research, 104, B8, 17911–17927.

Li, Y-L., Kohhauser, K.O., Cole, D.R., and Phelps, T.J. (2011) Mineral ecophysiological data provide growing evidence for microbial activity in banded-iron formations. Geology, 39, 707–710.

Little, C.T.S., Glynn, S.E.J., and Mills, R.A. (2004) Four-hundred and ninety-million-year record of bacteriogenic iron oxide precipitation at sea-floor hydrothermal vents. Geomicrobiology Journal, 21, 415–429.

Martinez, F., Taylor, B., Baker, E.T., Resing, J.A., and Walker, S.L. (2006) Opposing trends in crustal thickness and spreading rate along the backarc Eastern Lau Spreading Center: implications for controls on ridge morphology, faulting, and hydrothermal activity. Earth and Planetary Science Letters, 245, 655–672.

Parenteau, M.N. and Cady, S.L. (2010) Microbial biosignatures in iron-mineralized phototrophic mats at Chocolate Pots hot spring, Yellowstone National Park, United States. PALAIOS, 25, 97–111.

Peng, X., Zhou, H., Li, J., Li, J., Chen, S., Yao, H., and Wu, Z. (2010) Intracellular and extracellular mineralization of a microbial community in the Edmond deep-sea vent field environment. Sedimentary Geology, 229, 193–206.

Posth, N.R., Hegler, F., Konhauser, K.O., and Kappler, A. (2008) Alternating Si and Fe deposition caused by temperature fluctuations in Precambrian oceans. Nature Geoscience, 1, 703–708.

Quin, T.G., Long, G.J., Benson, C.G., Mann, S., Williams, R.J.P., 1988. Influence of Silicon and Phosphorus on Structural and Magnetic Properties of Synthetic Goethite and Related Oxides. Clays and Clay Minerals 36, 165–175.

Reysenbach A.L., Liu Y., Banta A.B., Beveridge T.J.,. Kirshtein J.D, Schouten S.,. Tivey M.K, von Damm K.L., and Voytek M.A. (2006) A ubiquitous thermoacidophilic archaeon from

Always consult and cite the final, published document. See http://www.minsocam.org or GeoscienceWorld

643 deep-sea hydrothermal vents. Nature, 442, 444–447.
644 Seehra, M.S., Roy, P., Raman, A., and Manivannan, A. (2004) Structural investigations of
645 synthetic ferrihydrite nanoparticles doped with Si. Solid State Communications, 130,
646 597-601.
647 Shannon, R.D. (1976) Revised effective ionic radii and systematic studies of interatomic distances
648 in halides and chalcogenides. Acta Crystallographica Section A, 32, 751–767.
649 Swedlund, P.J. and Webster, J.G. (1999) Adsorption and polymerisation of silicic acid on
650 ferrihydrite, and its effect on arsenic adsorption. Water research, 33, 3413–3422.
651 Takai, K., Nunoura, T., Ishibashi, J., Lupton, J., Suzuki, R., Hamasaki, H., Ueno, Y., Kawagucci,
652 S., Gamo, T., Suzuki, Y., Hirayma, H. and Horikoshi, K. (2008) Variability in the microbial
653 communities and hydrothermal fluid chemistry at the newly discovered Mariner
654 hydrothermal field, southern Lau Basin. Journal of Geophysical Research, 113, G02031,
655 doi:10.1029/2007JG000636.
656 Taylor, B., Zellmer, K., Martinez, F., and Goodliffe, A. (1996) Sea-floor spreading in the Lau
657 back-arc basin. Earth and Planetary Science Letters, 144, 34–40.
658 Toner, B.M., Santelli, C.M., Marcus, M.A., Wirth, R., Chan, C.S., McCollom, T., Bach, W., and
659 Edwards, K.J. (2009) Biogenic iron oxyhydroxide formation at mid-ocean ridge
660 hydrothermal vents: Juan de Fuca Ridge. Geochemica et Cosmochimica Acta, 73, 388–403.
661 Vempati, R.K. and Loeppert, R.H. (1989) Influence of structural and adsorbed Si on the
662 transformation of synthetic ferrihydrite. Clays and Clay minerals, 37, 273–279.
663 Vempati, R.K., Loeppert, R.H., Sittertz-Bhatkar, H., and Burghardt, R.C. (1990) Infrared
664 vibrations of hematite formed from aqueous- and dry-thermal incubation of Si-contanining
665 ferrihydrite. Clays and Clay Minerals, 38, 294–298.
666 Waychunas, G.A. (1991) Crystal chemistry of oxides and oxyhydroxides. In Oxide Minerals:
667 Petrologic and Magnetic Significance (D.H. Lindsley, ed.). Reviews in Mineralogy, 25,
668 11–68.
669 Yee, N., Phoenix, V.R., Konhuser, K.O., Benning, L.G., and Ferris, F.G. (2003) Chemical Geology,
670 199, 83–90.
671 Ying, F., Shui-li,Y., Yan-zhen, Y., Li-ping, Q., and Ban, H. (2007) Reaction mode between Si and
672 Fe and evaluation of optimal species in poly-silicic-ferric coagulant. Journal of

Always consult and cite the final, published document. See http://www.minsocam.org or GeoscienceWorld

673 Environmental Sciences, 19, 678–688.
674 Zachara, J.M., Kukkadapu, R.K., Peretyazhko, T., Bowden, M., Wang, C., Kennedy, D.W., Moore,
675 D., Arey, B., 2011. The mineralogic transformation of ferrihydrite induced by heterogeneous
676 reaction with bioreduced anthraquinone disulfonate (AQDS) and the role of phosphate.
677 Geochimica et Cosmochimica Acta 75, 6330–6349
678 Zhao, J., Huggins, F.E., Feng, Z., and Huffman G.P. (1994) Ferrihydrite: Surface structure and its
679 effects on phase transformation. Clays and Clay Minerals, 42, 737–746.
680 Zhou, H., Li, J., and Yang, Q. (2008) Microbiological oxidation of sulfide chimney promoted by
681 warm diffusing flow In CDE hydrothermal field in Eastern Lau Spreading Center, Eos Trans.
682 AGU, 89(53), Fall Meet. Suppl., Abstract B51D–0405.
683
684
685
686
687
688
689
690
691
692
693
694
695
696
697
698
699
700
701
702
703
704
705
706
707
708
709
710
711

Always consult and cite the final, published document. See http://www.minsocam.org or GeoscienceWorld

Table 1. Description of Fe-Si oxide samples from the Lau basin

Hydrothermal field	Sample	TVG NO.	Lat. (S)	Long. (W)	Depth (m)	Sample descriptions
Mariner	L9Y1	9	22º10'53"	176º36'06"	1922	Orange, loose, non-bedded
Mariner	L9Y2	9	22º10'53"	176º36'06"	1922	Bright yellow, loose, non-bedded
Mariner	L9Y3	9	22º10'53"	176º36'06"	1922	Yellow, loose, non-bedded
Vai Lili	L81	8	22º12'57"	176º36'26"	1744	Brown, layered, semi-consolidated
Vai Lili	L82	8	22º12'57"	176º36'26"	1744	Grey, loose, non-bedded
Vai Lili	L83	8	22º12'57"	176º36'26"	1744	White to grey, semi-consolidated
Hine Hina	L5Y1	5	22º32'01"	176º42'39"	1906	Yellow, layered, semi-consolidated
Hine Hina	L5Y2	5	22º32'01"	176º42'39"	1906	Yellow to brown, layered, semi-consolidated
Hine Hina	L6Y1	6	22º31'54"	176º42'56"	1877	Yellow, layered, semi-consolidated
Hine Hina	L6Y2	6	22º31'54"	176º42'56"	1877	Bright yellow, layered, semi-consolidated
CDE	L13Y1	13	20°41′11"	176°11′01"	2244	Red to brown, consolidated
CDE	L13Y2	13	20°41′11"	176°11′01"	2244	Bright yellow, semi-consolidated
CDE	L13Y3	13	20°41′11"	176°11′01"	2244	Orange, layered, semi-consolidated

Table 2. Frequencies and band assignments for the characteristic vibrations found in the IR spectra of Fe-Si oxide precipitates, Lau basin

Band	Wavenumbers (cm^{-1})	Assignments[a]
1	3545	ν_s Fe-OH
2	3390-3440	ν Si-OH
3	2360	ν C-O-C
4	1640	δ H-O-H
5	1002-1108	ν_sSi-O/Si-OH
6	942	ν Fe-O-Si
7	786	ν_s Si-O-Si
8	647	ν_s Fe-OH
9	460-472	ν_{as} Fe-O

[a] ν=stretching; δ=bending; *as*=asymmetric, *s*=symmetric

Table 3. Chemical compositions of the Fe-Si oxide deposits from Lau Basin analyzed by EMPA*

	Type I							Type II						
Oxide	1	2	3	4	5	6	Mean	7	8	9	10	11	12	Mean
SiO_2	63.64	52.33	33.47	66.01	34.26	30.31	46.67	81.63	69.84	88.54	88.64	82.8	87.15	83.1
P_2O_5	0.89	0.85	0.16	0.08	1.38	2.71	1.01	0.09	0.09	0.06	0.01	0.09	0.01	0.06
SO_3	0.3	0.25	0.19	0.08	0.2	0.48	0.25	0.07	0.02	0.05	0.21	0.1	0.03	0.08
Na_2O	0.21	0.31	0.39	0.08	0.21	0.36	0.26	0.06	0.32	0.13	0.13	0.23	0.11	0.16
MgO	0.3	0.37	0.21	0.41	0.17	0.46	0.32	0.05	0.59	<0.01	n.d.	0.01	0	0.11
Al_2O_3	0.01	0.03	0.02	<0.01	n.d.	0.05	0.02	0.1	12.63	0.02	0.02	0.01	0.02	2.13
K_2O	0.14	0.19	0.22	0.17	0.23	0.28	0.2	0.13	1.13	0.08	0.09	0.12	0.05	0.27
CaO	0.1	0.25	0.22	0.11	0.54	0.9	0.35	0.08	3.17	0.07	n.d.	0.1	0.11	0.59
TiO_2	n.d.	n.d.	n.d.	0.06	0.01	n.d.	0.01	0.15	0.5	n.d.	n.d.	n.d.	n.d.	0.11
Cr_2O_3	0.17	0.1	0.24	0.06	0.01	n.d.	0.1	0.06	0.05	0.24	n.d.	0.06	0.07	0.08
MnO_2	0.03	0	0	0.05	0.82	0.04	0.16	n.d.	0.2	0.05	n.d.	0.12	n.d.	0.06
Fe_2O_3	27.42	41.63	56.26	27.94	56.71	56	44.33	3.79	4.57	2.72	0.15	6.6	0.33	3.03
NiO	n.d.	0.04	0.08	n.d.	0.01	n.d.	0.02	0.01	0.02	n.d.	n.d.	<0.01	0.04	0.01
Total	93.21	96.36	91.47	95.06	94.55	91.57	93.7	86.21	93.11	91.95	89.25	90.21	87.9	89.77
Si:Fe[2)]	3.08	1.67	0.79	3.14	0.8	0.72	1.7	28.62	20.31	43.25	785.23	16.67	350.92	207.5

*: 1) n.d.-not detected; 2) molar ratios.

Figure Captions

Fig. 1. Regional bathymetric map and the study area along the Lau basin taken. Gridded bathymetric data sets are taken from British Oceanographic Data Centre (https://www.bodc.ac.uk/data/online_delivery/gebco/), using Global mapper v9.01 software.

Fig. 2. Selected XRD pattern of Fe-Si oxide (sample L6Y2). The numbers in brackets represent d-spacings in Ångströms. The green hump is the simulated main diffraction peak of opal-A, and the blue hump the simulated (110) diffraction peak of 2-line-ferrihydrite. The dash line represents the measurement baseline.

Fig. 3. Transmitted light photomicrographs of filamentous structures and bacterial meshes. (A) Filamentous Fe-Si oxides, sample L5Y2; (B) Orientated filaments roughly perpendicular to laminae, sample L6Y1; (C) Mesh of twisted and rod-like filaments with a septate structure (yellow arrows), sample L9Y1; (D) Mesh weaved by dendritic filaments, sample L13Y2.

Fig. 4. (A) Fe oxides occur as tiny spherules and as part of the larger amorphous mass indicative of the abiogenic precipitation, sample L5Y2. (B) Abiogenic spherules and amorphous masses apparently formed by biogenic filaments in the modern hydrothermal Fe-Si oxide deposit, sample L9Y3.

Fig. 5. SEM images of hydrothermal Fe-Si oxides. The yellow dots mark the EDS points (Fig. 6). (A) Filamentous structure of Fe-Si oxide, sample L5Y2; (B) *Leptothrix*-like straight sheaths, sample L6Y1; (C) Si-rich short rod-like filaments, sample L9Y2; (D) *Gallionella*-like twisted stalks, sample L81; (E) Cluster of Si-rich short rod-like or spherical structures, sample L9Y1; (F) Aggregates of tiny opal-A spheres encrusting the precursor filaments, L9Y2.

Fig. 6. Energy dispersive spectra of various Fe-Si oxides shown in Fig. 5. (A) filamentous Fe-Si oxide (Fig. 5A); (B) *Leptothrix*-like straight sheaths (Fig. 5B); (C) *Gallionella*-like twisted stalks (Fig. 5D); (D) Tiny sphere aggregate (Fig. 5F).

Fig. 7. TG-DTG-DSC curves of hydrothermal Fe-Si oxides from Lau Basin. (A) Sample L5Y2; (B) Sample L9Y2; (C) Sample L9Y3.

Fig. 8. XRD patterns of Fe-Si oxide (sample L5Y2) after being heated at 200, 450, 600, 800 and 1000 °C.

Fig .9. FTIR spectra of Fe-Si oxides. Samples numbers correspond to those in Table 1, and

numbers in parentheses represent bands, as assigned in Table 2.

Fig. 1.

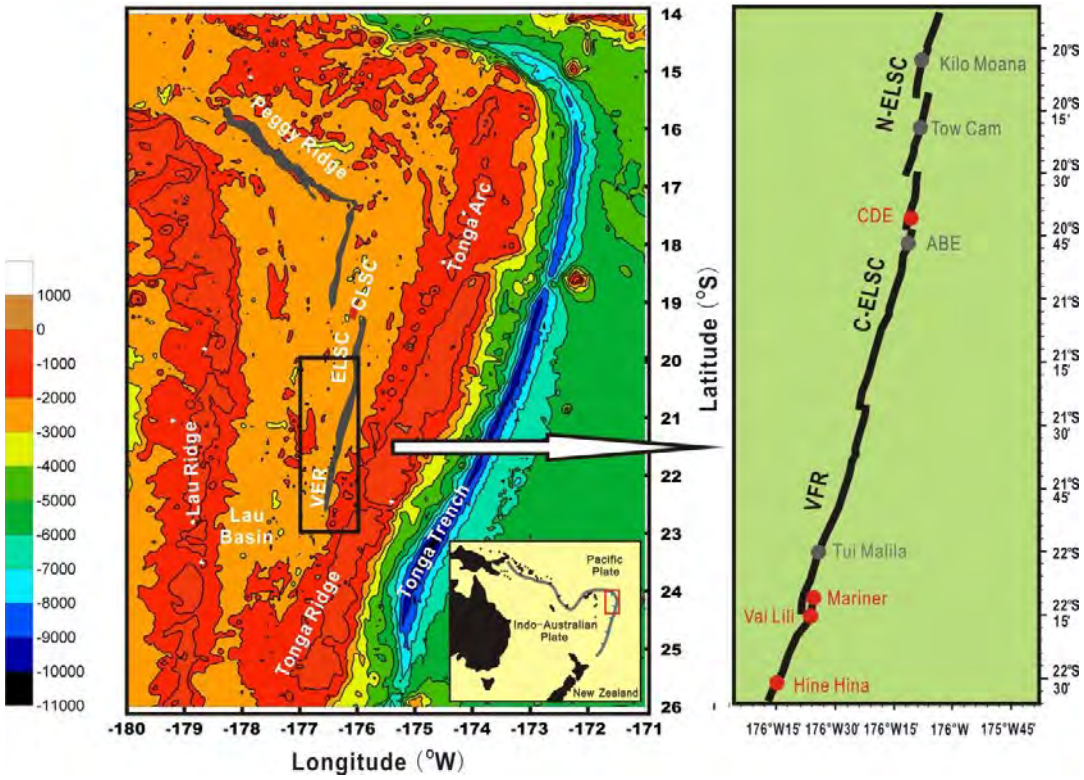

Fig. 2.

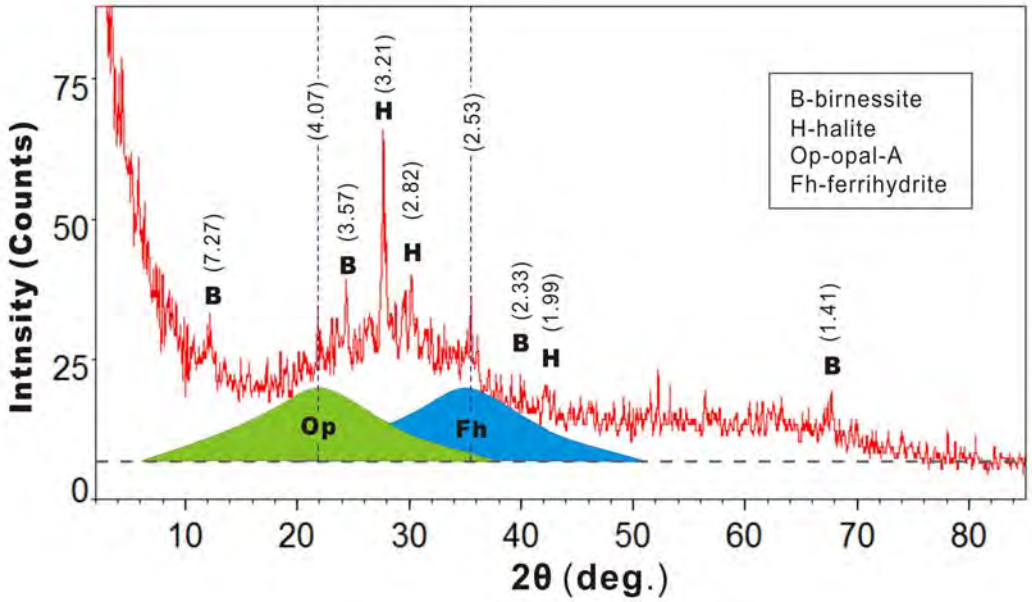
Intnsity (Counts)
2θ (deg.)
B-birnessite
H-halite
Op-opal-A
Fh-ferrihydrite
(7.27)
B
(4.07)
(3.57)
B
H (3.21)
(2.82)
H
(2.53)
B (2.33)
H (1.99)
B (1.41)
Op
Fh

Fig. 3.

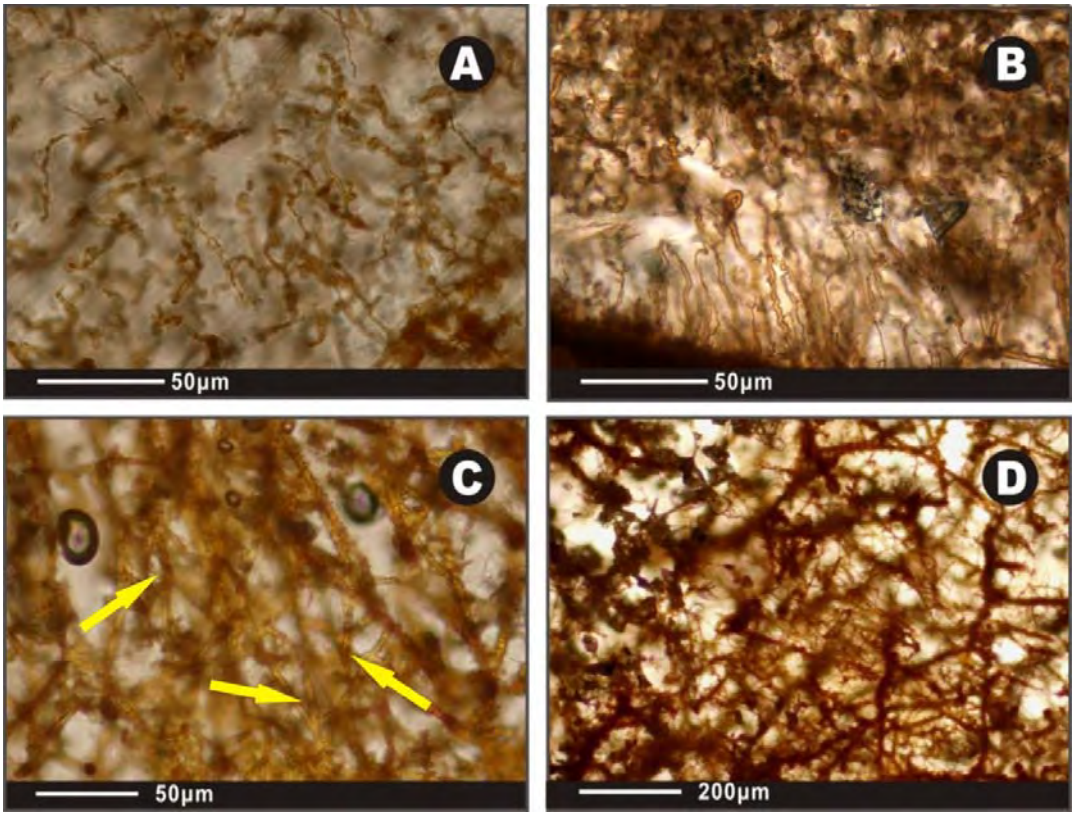

Fig. 4.

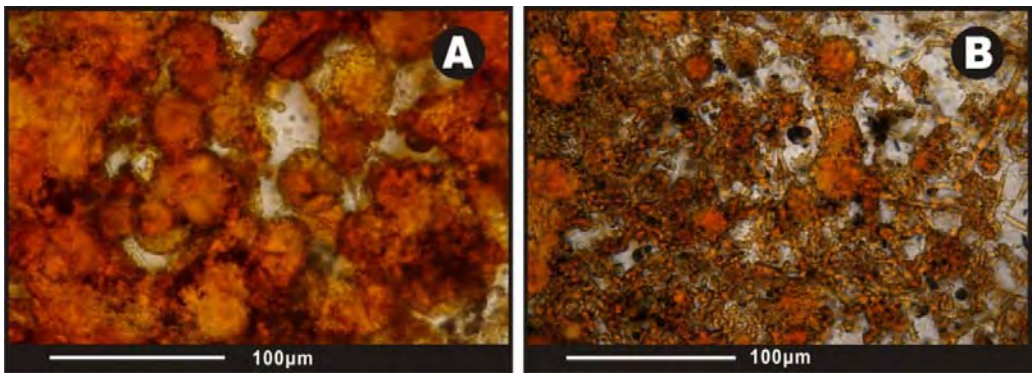

911
912
913
914
915
916
917 **Fig. 5.**

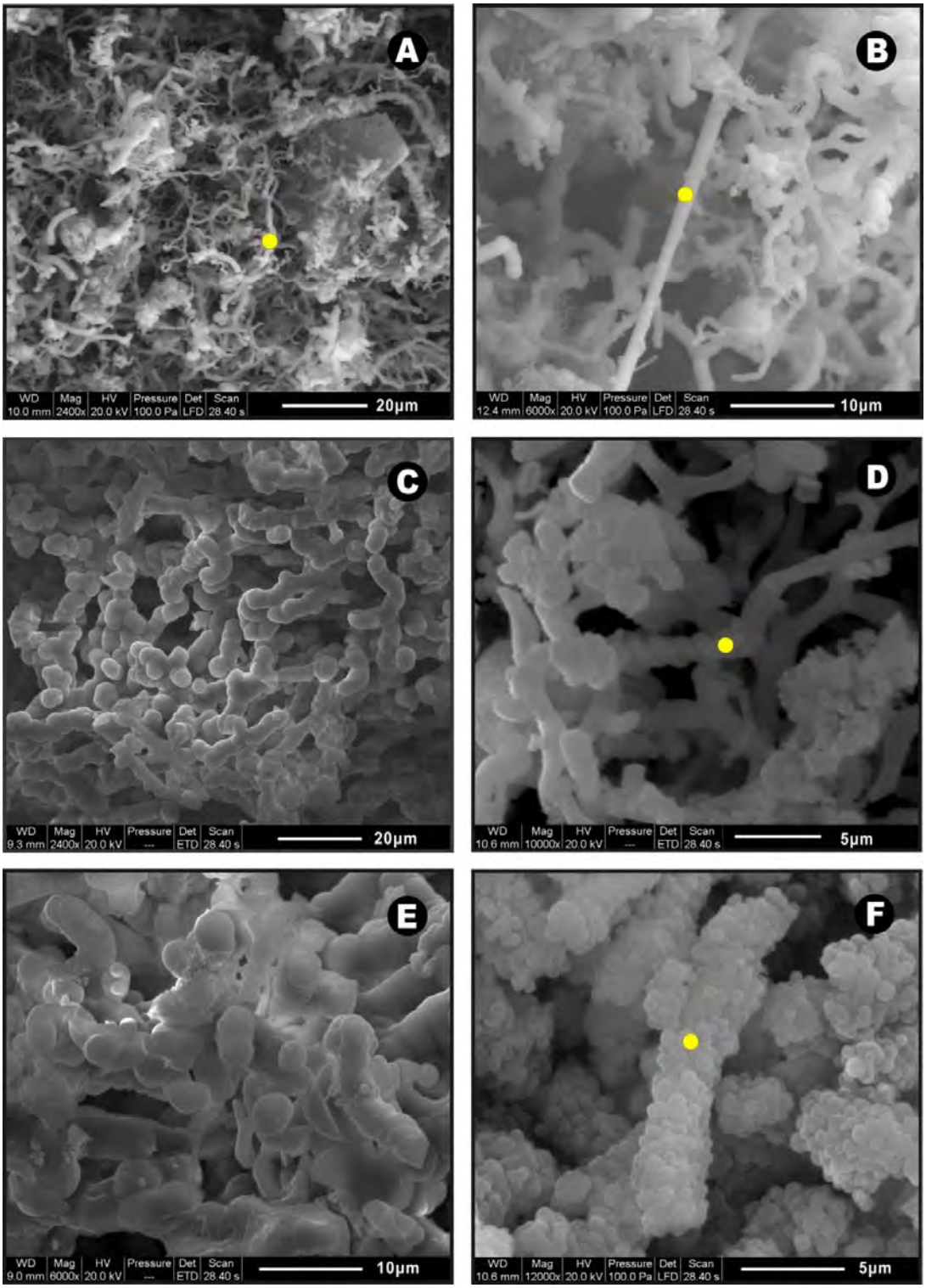
A
WD 10.0 mm | Mag 2400x | HV 20.0 kV | Pressure 100.0 Pa | Det LFD | Scan 28.40 s
20µm
B
WD 12.4 mm | Mag 6000x | HV 20.0 kV | Pressure 100.0 Pa | Det LFD | Scan 28.40 s
10µm
C
WD 9.3 mm | Mag 2400x | HV 20.0 kV | Pressure --- | Det ETD | Scan 28.40 s
20µm
D
WD 10.6 mm | Mag 10000x | HV 20.0 kV | Pressure --- | Det ETD | Scan 28.40 s
5µm
E
WD 9.0 mm | Mag 6000x | HV 20.0 kV | Pressure --- | Det ETD | Scan 28.40 s
10µm
F
WD 10.6 mm | Mag 12000x | HV 20.0 kV | Pressure 100.0 Pa | Det LFD | Scan 28.40 s
5µm

Fig. 6.

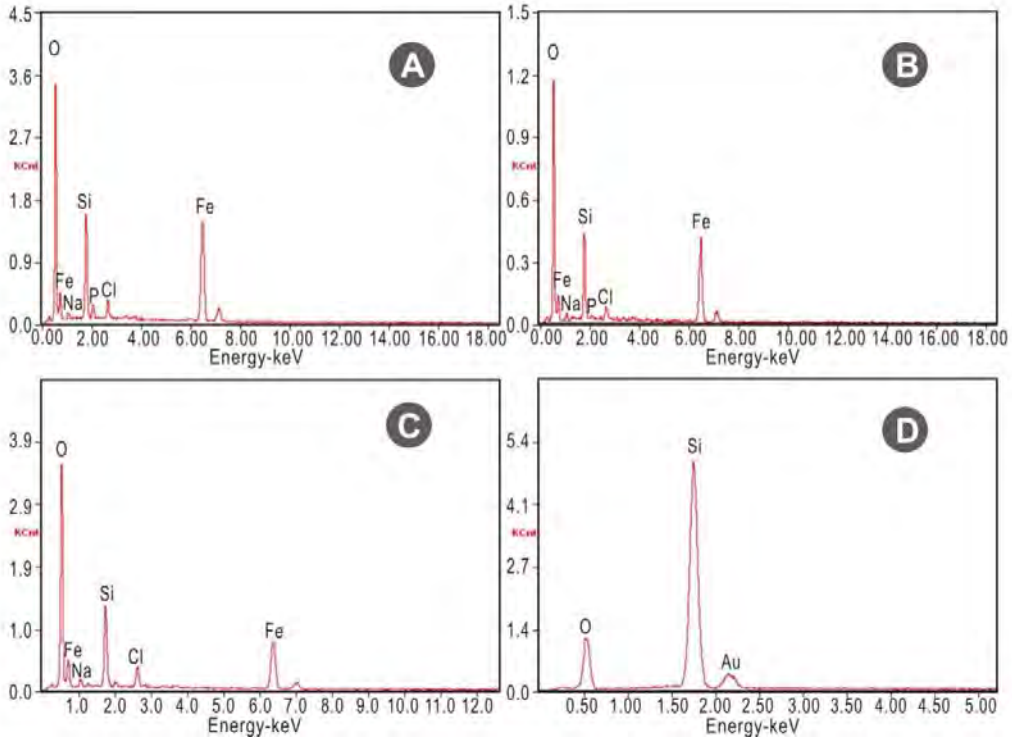
A
O
Si
Fe
Fe
Na
P
Cl
Energy-keV
B
O
Si
Fe
Fe
Na
P
Cl
Energy-keV
C
O
Si
Fe
Fe
Na
Cl
Energy-keV
D
Si
O
Au
Energy-keV

Fig. 7.

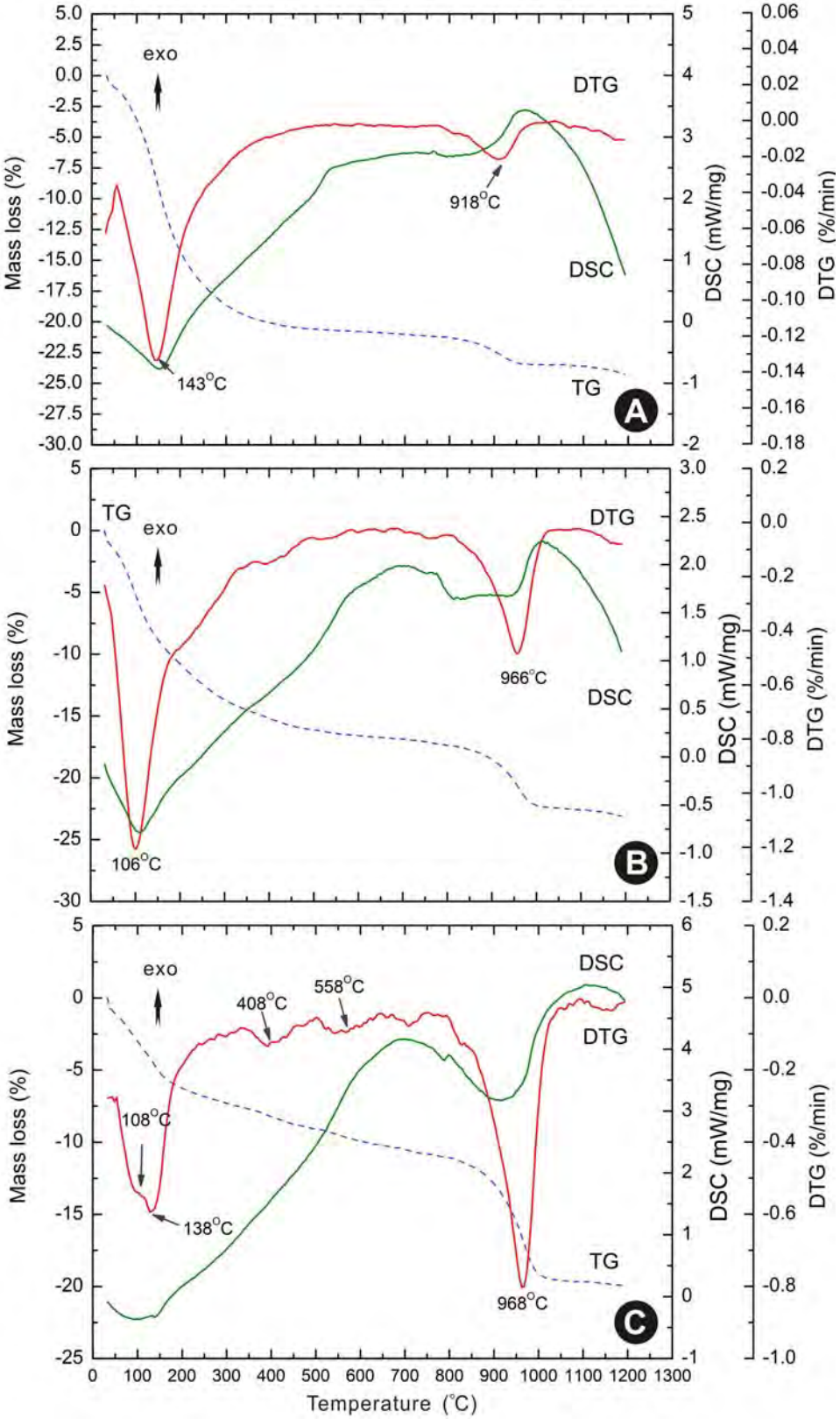
exo
DTG
DSC
TG
918°C
143°C
A
Mass loss (%)
DSC (mW/mg)
DTG (%/min)
TG
exo
DTG
DSC
966°C
106°C
B
exo
DSC
DTG
TG
408°C
558°C
108°C
138°C
968°C
C
Temperature (°C)

947

948

Fig. 8.

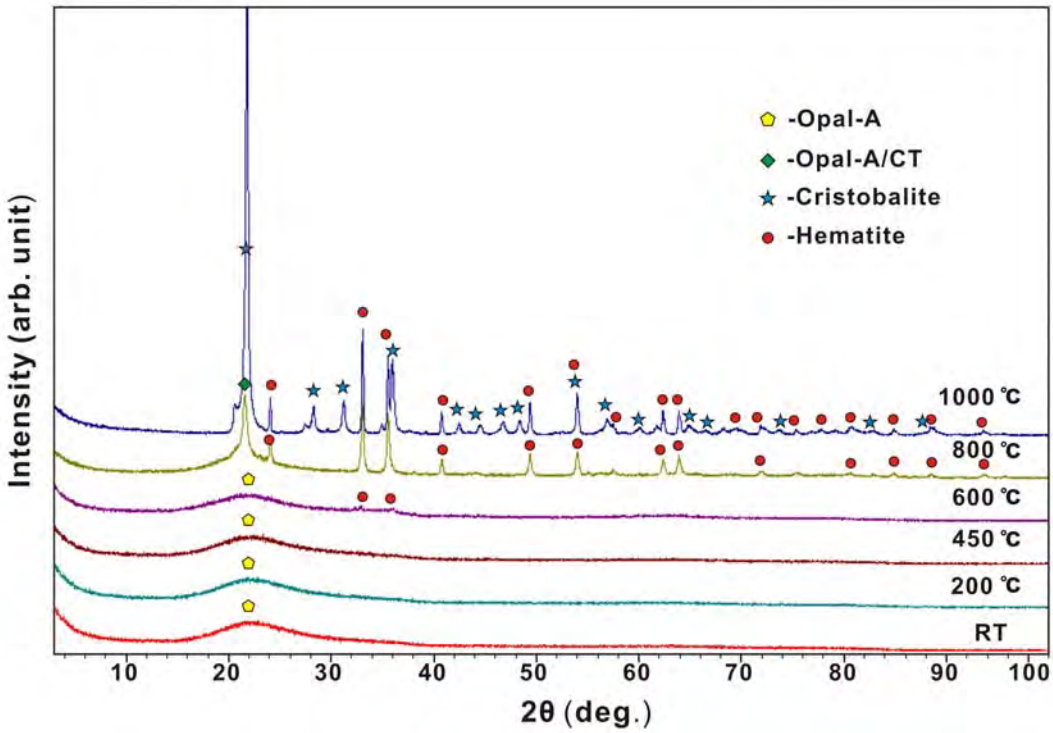
-Opal-A
-Opal-A/CT
-Cristobalite
-Hematite
1000 ℃
800 ℃
600 ℃
450 ℃
200 ℃
RT
Intensity (arb. unit)
10
20
30
40
50
60
70
80
90
100
2θ (deg.)

973

974 **Fig .9.**

975

976

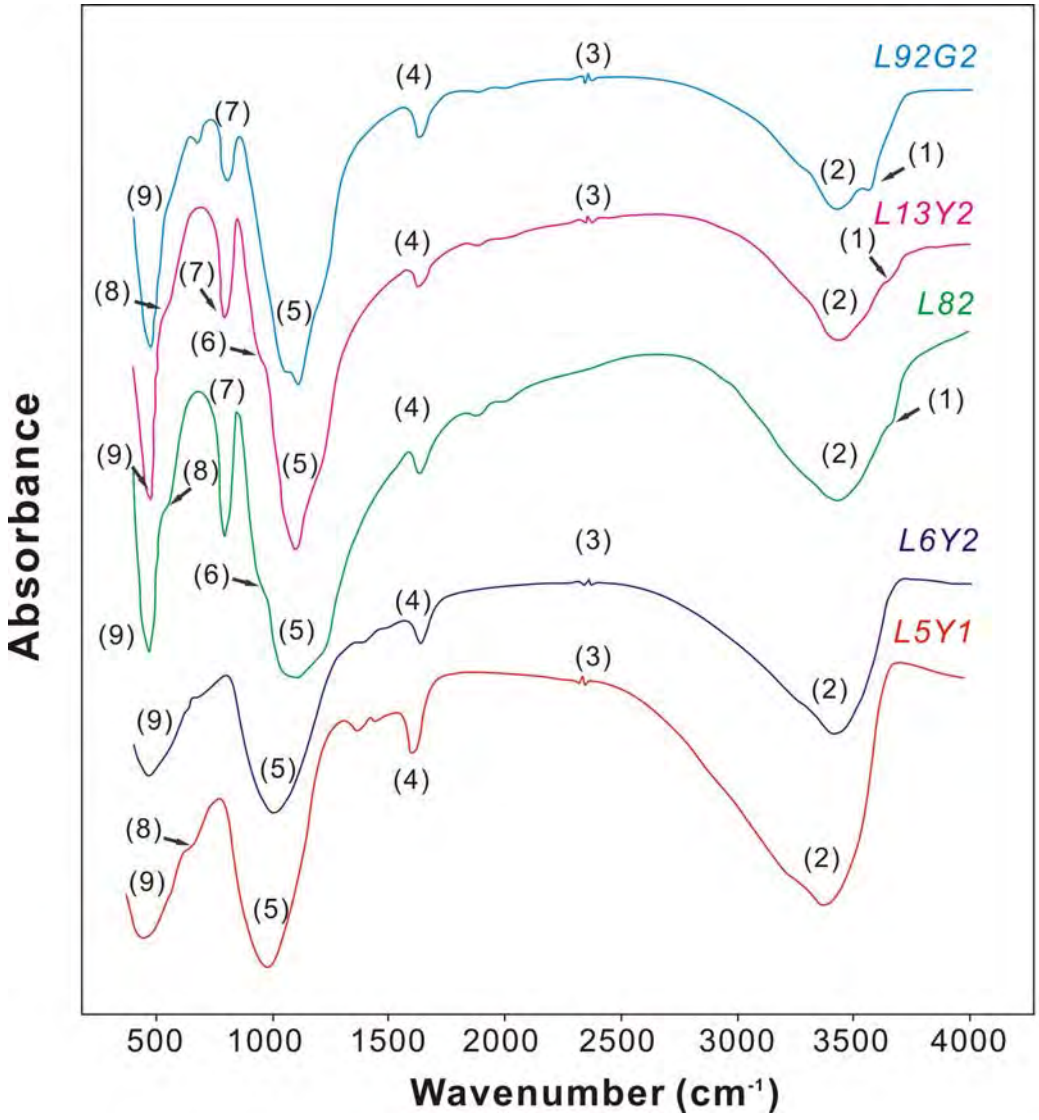

977